Technical Note

Cloud Seeding Evidenced by Coherent Doppler Wind Lidar

Jinlong Yuan [1,†]**, Kenan Wu** [1,†]**, Tianwen Wei** [1]**, Lu Wang** [1]**, Zhifeng Shu** [2]**, Yuanjian Yang** [2] **and Haiyun Xia** [1,2,3,4,*]

[1] School of Earth and Space Science, University of Science and Technology of China, Hefei 230026, China; yuanjinl@mail.ustc.edu.cn (J.Y.); wkn924@mail.ustc.edu.cn (K.W.); twwei@mail.ustc.edu.cn (T.W.); wanglu99@mail.ustc.edu.cn (L.W.)
[2] School of Atmospheric Physics, Nanjing University of Information Science and Technology, Nanjing 210044, China; 003373@nuist.edu.cn (Z.S.); yyj1985@nuist.edu.cn (Y.Y.)
[3] CAS Center for Excellence in Comparative Planetology, University of Science and Technology of China, Hefei 230026, China
[4] National Laboratory for Physical Sciences at the Microscale, University of Science and Technology of China, Hefei 230026, China
[*] Correspondence: hsia@ustc.edu.cn
[†] These authors contributed equally to this work.

Abstract: Evaluation of the cloud seeding effect is a challenge due to lack of directly physical observational evidence. In this study, an approach for directly observing the cloud seeding effect is proposed using a 1548 nm coherent Doppler wind lidar (CDWL). Normalized skewness was employed to identify the components of the reflectivity spectrum. The spectrum detection capability of a CDWL was verified by a 24.23-GHz Micro Rain Radar (MRR) in Hefei, China (117°15′ E, 31°50′ N), and different types of lidar spectra were detected and separated, including aerosol, turbulence, cloud droplet, and precipitation. Spectrum analysis was applied as a field experiment performed in Inner Mongolia, China (112°39′ E, 42°21′ N) to support the cloud seeding operation for the 70th anniversary of China's national day. The CDWL can monitor the cloud motion and provide windshear and turbulence information ensuring operation safety. The cloud-precipitation process is detected by the CDWL, microwave radiometer (MWR) and Advanced Geosynchronous Radiation Imager (AGRI) in FY4A satellites. In particular, the spectrum width and skewness of seeded cloud show a two-layer structure, which reflects cloud component changes, and it is possibly related to cloud seeding effects. Multi-component spectra are separated into four clusters, which are well distinguished by spectrum width and vertical velocity. In general, our findings provide new evidence that the reflectivity spectrum of CDWL has potential for assessing cloud seeding effects.

Keywords: Doppler wind lidar; spectrum skewness; cloud seeding; precipitation

1. Introduction

Cloud seeding is a common technique that changes the amount or type of precipitation, dispels fog, suppresses hail and weakens hurricanes [1–3]. Precipitation modification activities are usually performed by dispersing seeding agent particles into the air, which can increase cloud condensation or ice nuclei to enhance surface precipitation [4]. Cold clouds that contain supercooled liquid water (temperature below 0 °C) are seeded by silver iodide (AgI) [5], dry ice (frozen carbon dioxide) [6], and other agents [7–9]. The preferred agent is AgI, with a crystal structure similar to ice that can contribute to the freezing of supercooled water [10]. One method of cloud seeding is using ground-based burners, rockets, or cannons. The seeding agent is then launched into the upper part of the target cloud [11]. Another method uses aircraft flying around the target region and spraying seeders into the cloud [12,13]. The integrating autonomous unmanned aircraft system is applied to weather modification activities [14].

Direct observation of ice crystal formation and evolution is one of the most critical issues in supercooled stratus cloud seeding operations. It is still a challenge to

distinguishing between the impacts of cloud seeding and the natural variability of weather systems on the cloud-precipitation process [15], which requires multi-platform simultaneous observations [4,16]. For instance, only two of 36 experiments for seeding effects were confirmed by the research aircraft, radar, and surface instrumentation, mainly due to the natural fluctuations in ice crystal concentrations [17]. Radars are widely applied to obtain supercooled cloud seeding processes [5,18,19]. After AgI being released, the processes of supercooled liquid converting into ice particles, subsequent growing into precipitation are analyzed by combined with in-situ measurements and radar [20]. Satellites play an important role in detecting some seeding effects, such as Cloud-Aerosol Lidar and Infrared Pathfinder Satellite Observations (CALIPSO), Ice, Cloud, and land Elevation Satellite (ICESat) [21–25]. Other measurements such as polarization lidar [26–28], unmanned aerial vehicles [29], C- and W-band dual-polarization radars [30,31] can help ice cloud detection and the tracking of cloud seeding. The process of cloud seeding has strong complexity and variability in time and space. More detection methods need to be developed in order to obtain details of the cloud phase transformation and ice crystal evolution with high spatial and temporal resolution.

The Doppler wind lidar as an active optical remote sensing instrument measures the radial velocity accurately; these are primarily applied in detecting windshear [32], turbulence [33–36], aircraft vortex [37], fog [38,39], the atmosphere boundary layer [40], and gravity waves [41] under clear air conditions [42–45]. Recently, lidars have been extended to precipitation detection for their ability to detect the aerosol and precipitation signals simultaneously under rain conditions [46–50]. By deep analysis of the power spectrum, the CDWL can provide precise wind and rain detection with high spatial and temporal resolutions [51]. Based on accurate spectral measurements, the CDWL has the potential to reflect cloud phases, and thus it can be developed as a new way for cloud seeding detection.

In this work to support the cloud seeding operation, a CDWL was applied to detect wind, precipitation, and clouds simultaneously. The paper is organized as follows: the instruments are described in Section 2. In Section 3, the verification experiment using a CDWL and a MRR is presented. In Section 4, the application of the CDWL in a cloud seeding operation is presented. Finally, a conclusion is drawn in Section 5.

2. Instruments

A compact all-fiber CDWL system operating at an eye-safe wavelength of 1548 nm was used. The pulse duration and pulse energy of the laser was 200 ns and 110 μJ, respectively. The radial spatial resolutions were set at 30/60/150 m in the range of 0–2.5/2.5–5.5/5.5–13.0 km. The range-varying resolution is designed to improve the detection probability in the high altitude where the aerosol concentration is low. More detailed parameters and applications of the CDWL are introduced in previous work [41,47,51].

The MRR is a frequency modulated continuous wave (FMCW) radar (MRR-2, METEK GmbH). It operates at 24.23 GHz with a transmitting power of 50 mW. The main advantage of the MRR is that very small amounts of precipitation are detectable [52]. It provides profiles of drop size distribution, rain rate, falling velocity, and other precipitation parameters resolved into 30 range gates. In this study, the temporal and spatial resolution of the MRR was set as 1 min and 100 m, respectively.

3. Verification Experiment

The verification experiment was conducted at the campus of the University of Science and Technology of China, Hefei, China (117°15′ E, 31°50′ N). Measurements observed by the CDWL and MRR on 17 June 2019, 20 June 2019, and 12 July 2019 are shown in Figures 1 and 2, respectively.

The CNR represents signal intensity and determines the accuracy of other retrieved results, as shown in Figure 1a–c. Clouds are characterized by a steep increase of carrier-to-noise ratio (CNR) at the cloud base, followed by a strong decrease of CNR at the cloud

top. Spectrum broadening due to multiple scattering of clouds is observed, for instance, from 1:00 to 9:30 p.m., 20 June 2019 at an altitude of 0.5 km, as shown in Figure 1e. Spectrum broadening is obvious under precipitation for both aerosol and rain spectral components detected, as shown in Figure 1d–f. In addition, clear air turbulence, windshear, and aircraft wake lead to spectrum broadening due to strong velocity dispersion. Spectrum broadening due to multiple spectral components is more obvious than that of other factors, as statistically analyzed in [51]. The normalized skewness (Sk) is introduced to improve measurement of spectra shape, as in the following:

$$Sk = (M_r - M_l)/(M_r + M_l) \tag{1}$$

where

$$M_l = \int_{i=m-1}^{m-N} P(f_i)(f_m - f_i)^3 df \,, M_r = \int_{i=m+1}^{m+N} P(f_i)(f_i - f_m)^3 df \tag{2}$$

f_i and $P(f_i)$ are the Doppler frequency and power spectrum intensity at sampling point i, respectively. f_m is associated with the maximum signal intensity. The calculation contains $2N + 1$ samples around f_m, which are determined by the spectrum width and sample rate. The positive skewness means the spectrum is a right-tailed curve, and vice versa. Cubic spline interpolation can be pre-performed to smooth the spectrum curve and improve the robustness of the skewness calculation.
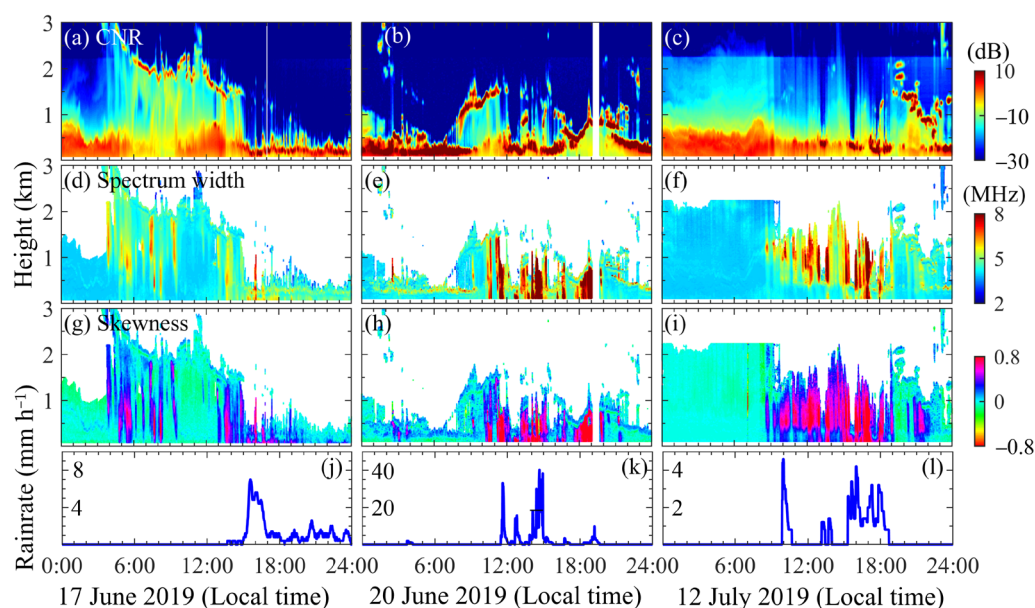

Figure 1. Precipitation processes observed by the CDWL on 17 June 2019, 20 June 2019, and 12 July 2019. (**a**)–(**c**) CNR. (**d**)–(**f**) spectrum width. (**g**)–(**h**) skewness. (**j**)–(**l**) surface rain rate provided by a Davis weather station.

The skewness deviates from 0 under precipitation, as shown in Figure 1g–i. Both spectrum width and skewness have vertical strip structures under the precipitation, similar to the MRR results shown in Figure 2. The spectrum skewness is more accurate to indicate precipitation with respect to the spectrum width. For instance, from 2:30 a.m. to 4:00 a.m. local time on 20 June 2019, the variation of spectrum width is not significant compared with that of skewness at an altitude of 0.1–0.5 km, while precipitation is detected by MRR. The precipitation time identified by the skewness is matched well with the real-time surface rain rate, as shown in Figure 1j–l. Precipitations at a high altitude of 0.5–2 km is detected by CDWL between 17 June 2019 and 12 July 2019. In these situations, the variation of skewness is significant at high altitudes, while little water is accumulated at the surface. Since the skewness is sensitive to the Doppler spectrum component, the

CDWL can be used to detect precipitation and cloud structures accurately when compared with MRR. The CDWL can reflect cloud characteristics, while the detection range is affected by cloud attenuation.
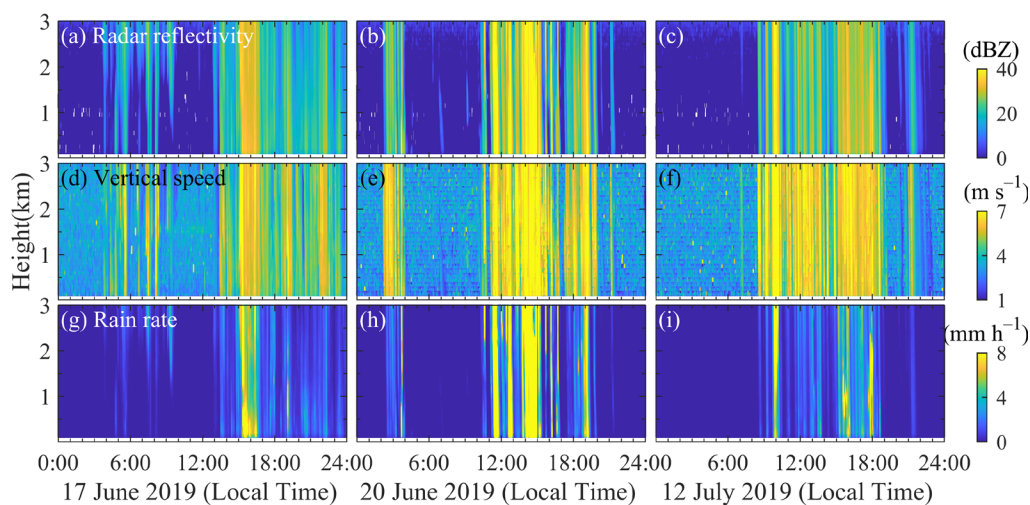

Figure 2. Precipitation processes observed by the MRR on 17 June 2019, 20 June 2019, and 12 July 2019. (**a**)–(**c**), radar reflectivity. (**d**)–(**f**) vertical velocity. (**g**)–(**i**) rain rate.

In order to illustrate the ability of the CDWL to identify spectral components, different types of Doppler spectra sampled from Figure 1 are shown in Figure 3. Figure 3a–c show the general spectrum in stable air conditions, the broadened spectrum due to the multiple scattering of clouds, and the Doppler spectrum with spectrum broadening due to turbulence at 12:00 p.m., respectively. Figure 3d–l shows different types of Doppler spectra during precipitation as identified by skewness. In detail, Figure 3d–h exhibit Doppler spectra with distinct double-peak distribution, which are easy to separate into aerosol and raindrop components with double-peak fitting. Figure 3i, j presents biased unimodal structures with spectrum broadening, in which overfitting may occur and cause misleading results for too many freedom degrees in double-peak fitting. To address it, it is necessary to reduce the scope of the fitting solutions by restrictions. Union double-peak fittings are applied with fixed $f_a - f_r$ to separate aerosol and rain components for these overlapped spectra at the same altitude, because the main difference of Doppler velocity is caused by vertical velocity.

Figure 3k, l shows biased single-peak Doppler spectra with small spectrum broadening, indicating that the signal intensity of one component is significantly weaker than that of the dominating component. The hidden peak is searched for using the residual spectrum between the observed spectrum and a Gaussian spectrum [46]. Compared with spectra shown in Figure 3d–j, the spectrum broadening is not obvious in Figure 3g, h, k, l, while the normalized skewness significantly deviates from 0.

The verification experiment indicates that the CDWL shows a good performance in power spectra measurement. Different types of components can be accurately identified and separated by multiple parameters derived from lidar spectra, which are useful for studying aerosol, precipitation, and clouds.
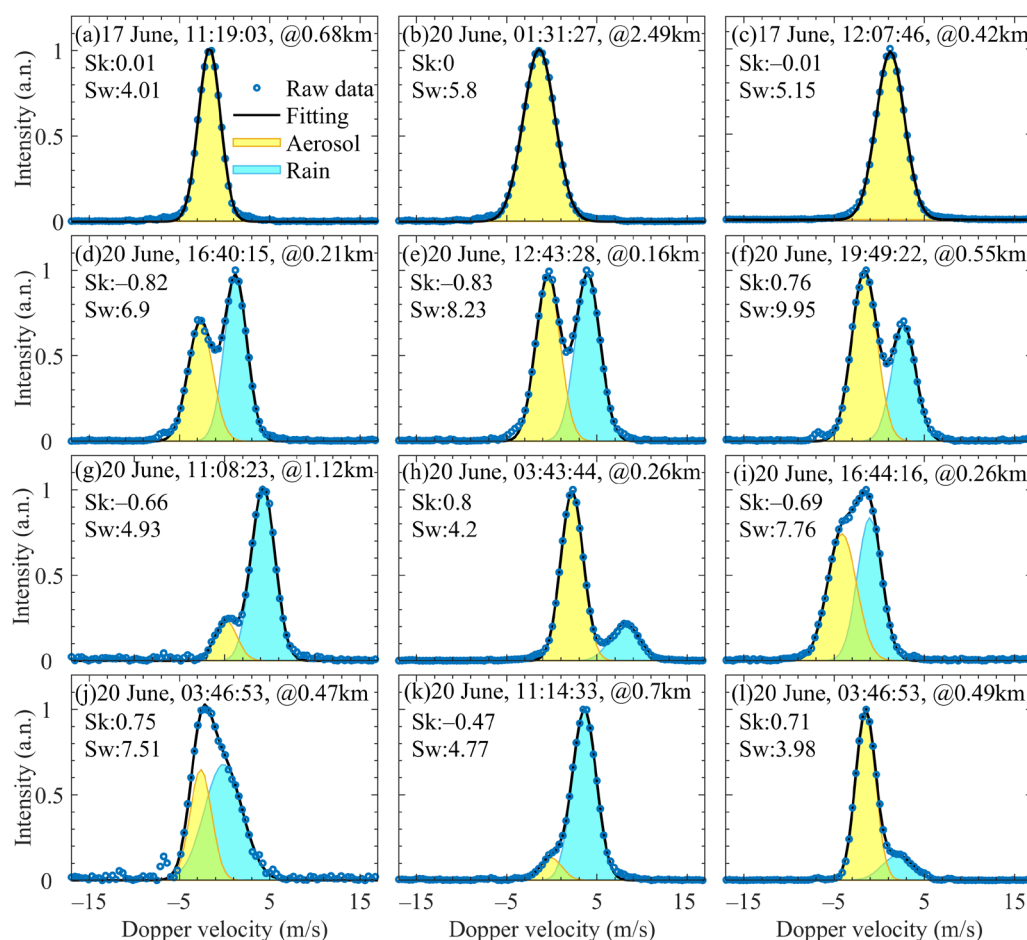
Figure 3. Examples of different types of Doppler spectra. (**a**) General aerosol spectrum; (**b**) cloud spectrum; (**c**) spectrum under strong turbulence; (**d**)–(**l**) precipitation spectra and its separation results. Circles stand for the raw data of spectra. Black lines represent fitting results. The yellow shadow and light blue shadow represent separated aerosol and rain components, respectively.

4. Application in an Artificial Precipitation Operation

The method was integrated into the CDWL to support the cloud seeding operation. The field experiment was performed at an airport of Xilin Gol grassland, Inner Mongolia, China (112°39′ E, 42°21′ N), from 28 August to 1 October 2019. The velocity azimuth display (VAD) technique was used to retrieve the vertical wind profile. The lidar operated in the VAD scanning mode with an elevation angle of 60° and a period of 2.5 min. The VAD technique was used to retrieve the vertical wind profile. The azimuth angle scanned from 0° to 300°, with an angle step of 5°. The CDWL results of cloud, precipitation, windshear, and turbulence intensity during the experiment are given in [51,53].

A cloud seeding event was conducted locally to accelerate the development of the precipitation process within the clouds. The cloud seeding operation started at 5:30 p.m. local time, 12 September 2019. The seeding was conducted by burning about 60 silver iodide cigarette strips carried by five aircraft. Each strip weighed 4.2 kg, including 125 g of silver iodide. Aircrafts seeded AgI into the cold cloud from the altitude of 4.0–4.5 km to help increase the probability of ice crystal formation and growth into precipitation hydrometeors.

The cloud phase is provided by the Advanced Geosynchronous Radiation Imager (AGRI) in FY4A satellites [54], with a spatial resolution of 4 km, as shown in Figure 4. Figure 4a shows the cloud phase across the China region at 5:30 p.m. local time. The seeding was conducted by the five aircraft simultaneously in the target region, which is represented by the yellow square in Figure 4a. Cloud phase distribution of seeding regions at

different times are shown in Figure 4b–e. The black triangle indicates the location of the CDWL. The orange arrows represent the wind vector. Mixed clouds were dominant at the beginning of seeding operation, as shown in Figure 4a. Then the obvious growth of ice crystals was detected after the seeding near the lidar location.
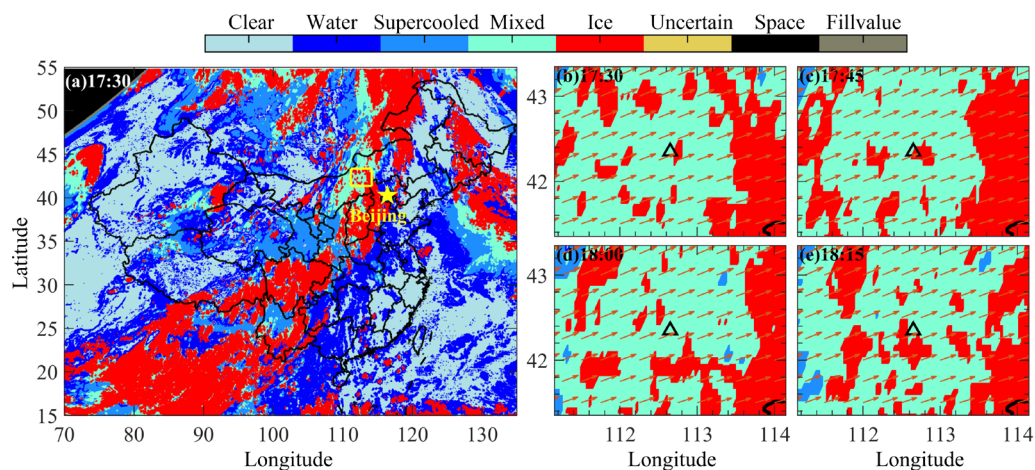

Figure 4. Cloud phase provided by FY4A satellite in 12 September 2019, local time. (**a**) shows the cloud phase across the China region at 5:30 p.m. local time, the yellow square indicates the seeding region. (**b**)–(**e**) show cloud phase distribution of seeding regions at different times. The black triangle indicates the location of the CDWL. The orange arrows and black triangle represent the wind vector and the location of the CDWL, respectively.

Atmospheric profiles provided by the microwave radiometer (MWR) are shown in Figure 5. Application and detail specifications of the MWR are provided in [51]. Temperature, water-vapour, and liquid water content of the seeding region at 5:30 p.m. were −5.8~−9.3 °C, 2.5–3.2 gm^{-3}, and 0.12–0.15 gm^{-3}, respectively. Temperature and water-vapour were decreasing while liquid water content was increasing after the seeding operation. The liquid water content reached 1.22 gm^{-3}, when precipitation occurred.
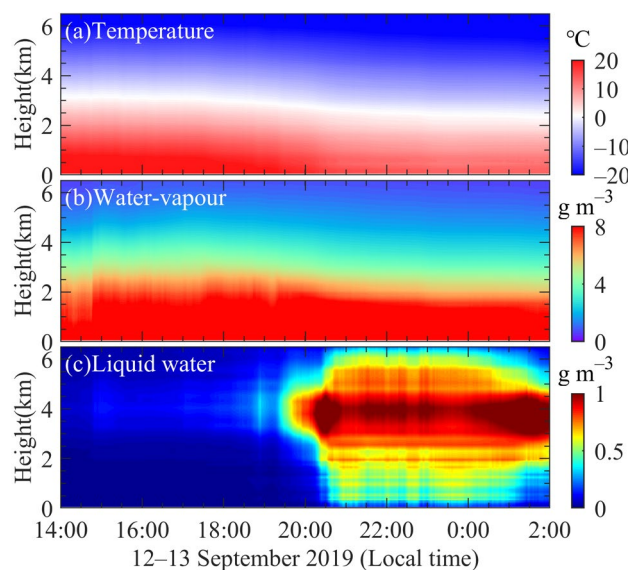

Figure 5. Continuous MWR observation results during 12–13 September 2019.

The cloud seeding is documented by the CDWL, as shown in Figure 6. The cloud base is marked by black circles in Figure 6a. The cloud and wind speeds are shown in Figure 6d–f, which are retrieved by single peak fitting. The detection of the cloud

boundary and its velocity contributed to determine the time and position of the seeding operation. Before the cloud seeding, the cloud base moves downward from about 6 km to 3 km. During the cloud seeding, the CNR at 4.0–4.5 km altitude was increased from 5:30 p.m. to 6:00 p.m. local time. The corresponding vertical velocity had significant changes in the ice region near 4 km, as shown in Figure 6f. The injection of AgI particles into a supercooled cloud layer released latent heat, forming buoyancy in the ice-affected region [4,13]. Thus, a small-scale and persistent updraft airflow was accompanied by downdrafts on the outside edges [55]. There was a vacancy region in the ice-affected region near 6:00 p.m. local time. It might be that rising and descending airflow were neutralized, causing the cloud water to erode by evaporation, and leading to formation holes in clouds [56].
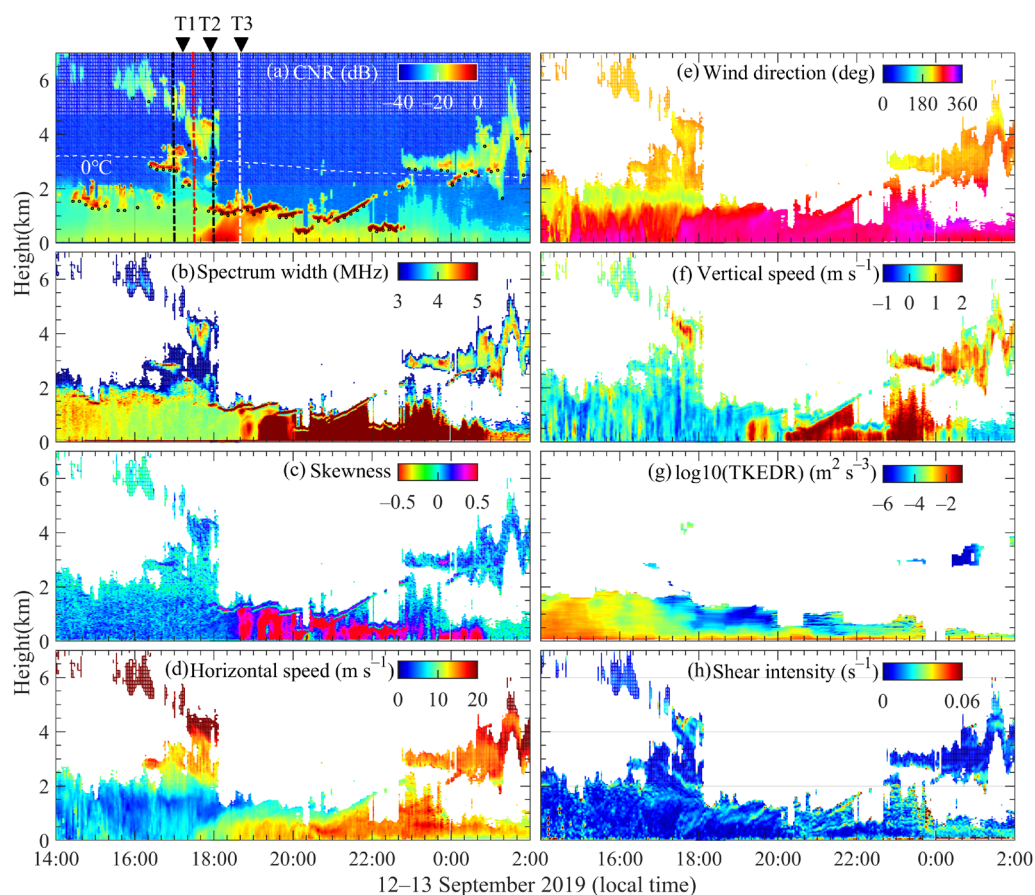

Figure 6. A cloud seeding operation process detected by CDWL during 12–13 September 2021. (**a**) CNR, (**b**) spectrum width, (**c**) skewness, (**d**) horizontal wind speed, (**e**) horizontal wind direction, (**f**) vertical wind velocity, (**g**) turbulent kinetic energy dissipation rate (TKEDR), (**h**) shear intensity. The TKEDR is used to estimate turbulence intensity [35]. The vertical red dash-dotted line in (**a**) represents the moment (5:30 p.m.) when seeding begins. The vertical black dash-dotted line represents the moments half an hour before and after seeding. The vertical white dash-dotted line stands for the moment (6:40 p.m.) when precipitation begins.

After the seeding began, the CNR at the 0–1.5 km altitude was increased from 5:30 p.m. to 7:00 p.m. local time (Figure 6a). There was a large amount of silver iodide-type aerosols in the boundary layer via wet deposition over large areas [57], which were not completely injected into the cloud environment. These silver iodide-type aerosols were washed out near the atmospheric boundary layer (ABL), with variation of wind speed and direction, which served as an inadvertent transporter of the seeding agent that sometimes happens in weather modification practices [58]. The lidar using VAD scanning can only detect the seeding particles in the inverted cone. Low altitude particles are detected at first, and then higher altitude particles can be detected with particle transport. Silver

iodide-type aerosols might serve as cloud condensation nuclei (CCN) and thus have a substantial effect on cloud properties and the initiation of precipitation [59–61]. After a while, the precipitation began (6:40 p.m.), which can be seen from the broadened spectrum width and increased skewness in Figure 6b, c, indicating the positive effectiveness of the cloud seeding. The airport was experiencing strong winds, with ground-level wind speed exceeding 15 m/s frequently, as shown in Figure 6d. It can easily produce wind shear and turbulence, which may threaten the safety of aircraft operation. For instance, strong low-level jets were detected during the experiments, as presented in [51]. Therefore, an important role of lidar is to provide windshear and turbulence alerts, as shown in Figure 6g, h.

Phase transformation and precipitation formation in seeded clouds are associated with the Wegener-Bergeron-Findeisen (WBF) process. The equilibrium vapor pressure of water vapor with respect to ice is less than that with respect to liquid water at the same subfreezing temperature [62]. Before cloud seeding, supercooled liquid water and ice crystals coexist in mixed phase clouds, but the concentration of natural ice nuclei is very small. There is a competitive relationship between the rate of generation and scavenging of supercooled liquid water in the target region [63]. After the seeding flight, AgI particles are injected into supercooled water supplying a large number of tiny artificial ice nucleus, and the process of supercooled liquid water scavenging by evaporation and vapor condensing into ice crystals is greatly strengthened. Thus, the ice crystals would gain mass by vapor deposition, at the expense of the supercooled water that would lose mass. Upon attaining sufficient weight, the ice crystals would fall. As altitude descends with temperature gradually increasing, the ice crystals generate liquid cloud droplets by melting. Subsequently, a mixed layer is formed, which makes the lidar signal difficult to penetrate, as shown in Figure 6a. In particular, the cloud spectrum width and skewness after seeding have a two-layer structure, and this continues for several hours, as shown in Figure 6b, c. The skewness of the lower layer (cloud base) is close to 0, with little spectrum width broadening, indicating that the lower layer is comprised of liquid cloud droplets. However, the skewness of the upper layer deviates from 0, with obvious spectrum width broadening, indicating that multiple components are mixed in this layer. This mixed layer might contain big cloud droplets, raindrops, melting ice particles, graupels, and small hail [59,61].

In order to investigate specific components of the mixed layer, these multi-component spectra including mixed cloud spectra and precipitation spectra are identified by skewness. Then Doppler velocity and spectrum width are separated from these spectra by two-peak fitting, as demonstrated in Section 3. For the precipitation spectrum, the left peak with smaller Doppler velocity is grouped as cluster A (aerosol component), and the corresponding right peak with larger Doppler velocity is grouped as cluster B (raindrop component) [47,51]. For the mixed cloud spectrum, the left and right peaks are grouped as cluster C and cluster D. Then, velocity components are retrieved from Doppler velocity, using the filtered sine wave fitting (FSWF) method [64], as shown in Figure 7. The horizontal speed and direction of spectrum components are close because of the drag effect, as shown in Figure 7b, c, f, g. The spectrum width and vertical velocity of cluster C are different from these of cluster D, but close to these of cloud base, as shown in Figure **7**a, d. It indicates that cluster C is comprised of liquid cloud droplets as well.
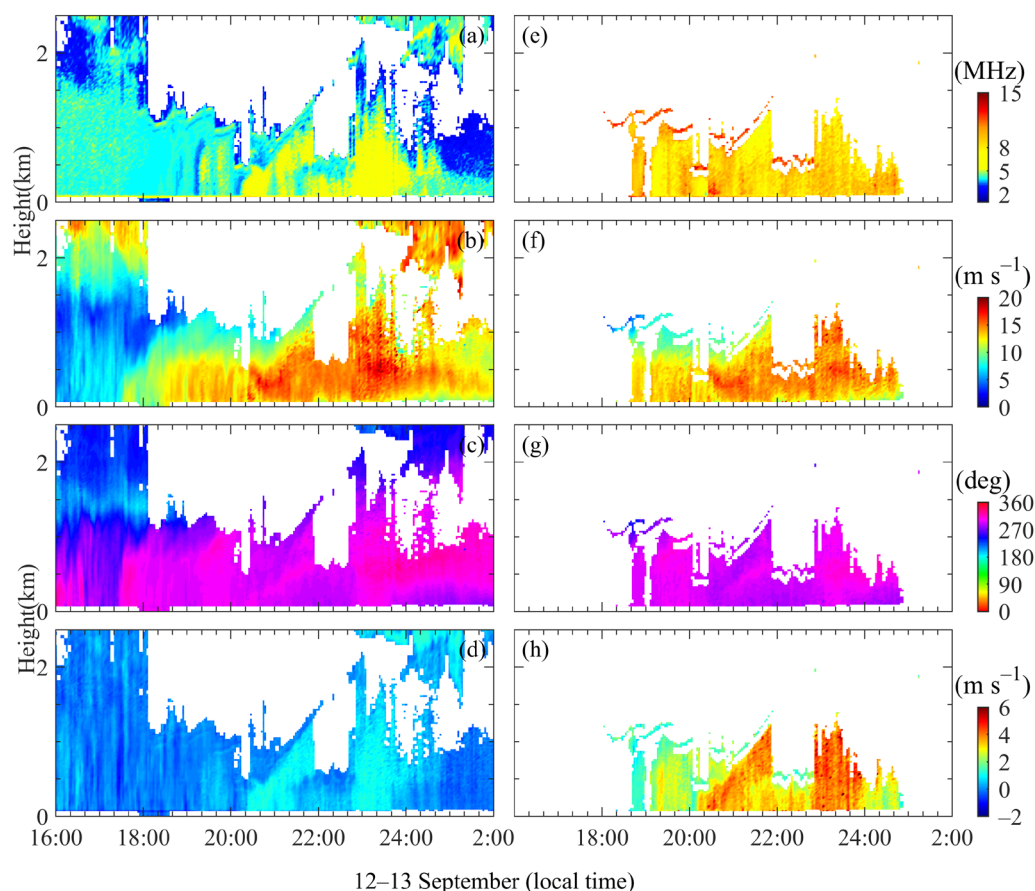
Figure 7. (**a**) The spectrum width of aerosol and cluster C; (**b**) horizontal speed of aerosol and cluster C; (**c**) horizontal direction of aerosol and cluster C; (**d**) vertical velocity of aerosol and cluster C; (**e**) the spectrum width of raindrop and cluster D; (**f**) horizontal speed of raindrop and cluster D; (**g**) horizontal rain direction of raindrop and cluster D; (**h**) vertical velocity of raindrop and cluster D.

To analyse the differences of these clusters, the density distribution of the spectrum width and vertical velocity are shown in Figure 8. These four clusters can be clearly distinguished from Figure 8. Distributions of the aerosol and raindrops are consistent with the result in [51]. There is a slight decrease in speed (0.9 m/s) and spectrum broadening (5.2 MHz) in aerosol in the precipitation condition. The spectrum width and vertical velocity of cluster C (cloud droplet) are concentrated at 0 m/s and 4.0 MHz. The characteristics of cluster D are significantly different from raindrops below the cloud base. The spectrum width of cluster D is concentrated at 11.2 MHz, which is larger than that of the raindrops (8.4 MHz). The vertical velocity of cluster D is concentrated at 1–2 m/s, while that of raindrop is concentrated at 3–4 m/s. It is consistent with results of cloud ice and liquid precipitation observed in [30,65]. Cluster D falls faster than cluster C, which is similar to the general mixed-phase cloud results observed by aircraft [66] and remote sensors [65,67]. Thus, cluster D is likely to be cloud ice (crystal, graupel or small hail) [59]. Another possible explanation is that ice particles melt gradually when they fall through layers warmer than 0 °C. The ice particle is wrapped in water, which has a larger vertical velocity and wider particle spectrum distribution than cluster C. But these melting ice particles fall more slowly than raindrops with the same mass [68]. Similar to the relation between aerosol and rain, the vertical velocity of the cluster D is larger than that of small cloud droplets [69].
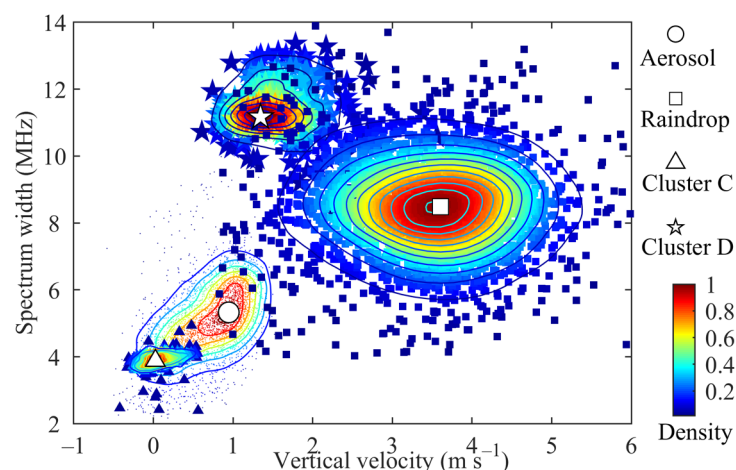
Figure 8. The density distribution of the spectrum width and vertical velocity. The circle, square, triangle, and pentagram represent aerosol, raindrops, and clusters C and D.

If it's drizzling below the cloud, it still has skewness increasing and spectrum width broadening, unless the weaker component is completely submerged by the stronger one. Generally, aerosol signals are dominant in the early stage of drizzling, and raindrops are dominant later as aerosols are washed. If the liquid layer is below the cloud, the power spectrum is symmetric with little skewness. A notable feature of the liquid water layer below the cloud is that the reflection signal intensity is significantly greater than that of drizzling. Clouds are usually extracted first by CNR, using the Haar wavelet covariance transform (HWCT) algorithm [51]. Examples of detected cloud spectra from cloud middle to cloud base are shown in Figure 9. Figure 9a–c show cloud spectra before cloud seeding at T1 (5:17 p.m.). That cloud is in liquid phase with skewness close to 0. In Figure 9e, f, i, j, cloud spectra extracted from the upper layer have largely normalized skewness and spectrum width, which indicates that multiple components exist. It is probable that cloud seeding generates a large number of ice crystals [70], resulting in big cloud droplet or that raindrops coexist below the melting layer [71]. Considering that cluster D falls slower than raindrops, it also could be that cloud seeding intensified the process of cloud-precipitation and generated graupel or small hail [59]. As the altitude continues to decrease, the reflection strength of cluster D decreases and cloud droplet dominates, as shown in Figure 9f, j. Only the cloud droplet exists at the cloud base with small normalized skewness and spectrum width, as shown in Figure 9g, k, which subsequently produces precipitation (Figure 9l). This change process is very similar to the melting layer detected by radar [30].

Applications of the lidar in cloud seeding are summarized into three aspects: (1) as an auxiliary measurement for cloud monitoring before operation., the lidar can well identify the cloud base and even penetrate the cloud when the cloud layer is thin. The cloud velocity provided by the lidar is useful for the preliminary preparation of cloud seeding; (2) providing windshear and turbulence alerts. The site is prone to windy weather, and the lidar plays an important role in ensuring safety of aircrafts during operation, especially in taking off and landing; and (3) tracking the cloud seeding, which is the focus of this paper. First, the transport of AgI leads to a significant increasing of CNR in the ABL after seeding, which proves that the detection range of lidar is within the seeding influence region. And changes in CNR and vertical velocity are detected at 4.0–4.5 km altitude. Similar to the linear polarization ratio related to the ratio of ice to water particle concentration, which is used to reflect ice-water balance due to seeding effects [26,27], the CDWL spectrum also reflects the change of cloud phase to a certain extent. The spectrum width and skewness of cloud show a two-layer structure below 0 °C contour, which is similar to the melting layer structure. Combining characteristics of separation components, it could be inferred that seeding enhanced the development of the precipitation process, resulting in the detection of the two-layer structure at such a low altitude. Therefore, the CDWL

provides multiple measurements, such as CNR, wind field, spectrum width, skewness, and separated components, which are indicated to be quite useful supplements for cloud seeding detection.
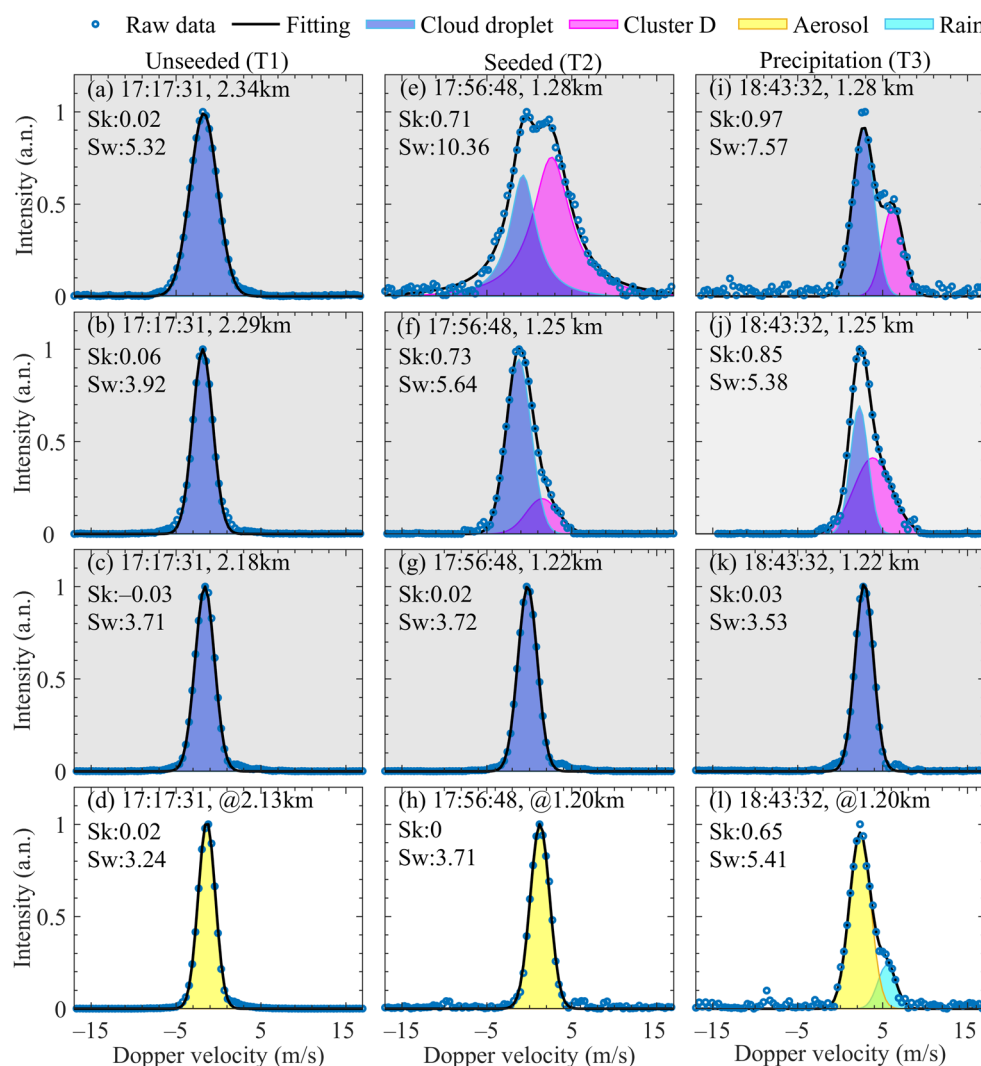

Figure 9. Examples of cloud spectra from cloud middle to cloud base. (**a**)–(**c**) show cloud spectra of unseeded at T1 (5:17 p.m.); (**e**)–(**g**) show cloud spectra of after seeded at T2 (5:56 p.m.); (**i**)–(**k**) show cloud spectra at T3 (6:43 p.m.), when precipitation formed. (**d**), (**h**), (**l**) are aerosol or precipitation spectra below cloud base. Circles stand for the raw data of spectra. Black lines represent fitting results. The light purple shadow and pink shadow represent separated cloud droplet and cluster D, respectively. The yellow shadow and light blue shadow represent separated aerosol and rain components, respectively.

5. Conclusions

In this study, a method based on spectra analysis using a CDWL was developed for cloud-precipitation measurements, incorporating satellite and MWR. Multiple parameters derived from the lidar power spectrum provide potential evidence for the cloud-seeding effect. Transport of seeding particles in the ABL and cloud changes are characterized by CNR and velocity at the early stages of the seeding. Although the clouds were not penetrated completely, the two-layer structure of normalized skewness and spectrum width is detected in the layer warmer than 0 °C after seeding, which is similar to the melting layer structure. Multi-component spectra including cloud and precipitation are separated into four clusters, which have distinguishable distribution characteristics of spectrum width and vertical velocity. Clusters from the multi-component spectrum of cloud

might be cloud water or melting ice, which is possibly related to a large amount of ice crystals produced by cloud seeding. Nevertheless, our findings provide evidence that CDWL has potential in monitoring the microphysical process of cloud-precipitation due to cloud seeding. With these multiple parameters retrieved from the lidar spectrum, the lidar can be extended to the research of melting layer characteristics, cloud phase identification, and classification, which is important for climate models, weather modification, and aviation safety. In future work, we will try to improve cloud penetration ability by increasing the power of the laser to study the cloud seeding process combined with other measurements. We also plan to integrate polarization detection into the lidar system[72].

Author Contributions: Conceptualization, H.X.; Methodology, J.Y. and K.W.; Software, J.Y.; Formal Analysis, H.X., J.Y., and K.W.; Investigation, J.Y.; Resources, J.Y.; Data Curation, J.Y.; Writing—Original Draft Preparation, J.Y., and K.W.; Writing—Review & Editing, T.W., L.W., Z.S. and Y.Y.; Visualization, J.Y.; Supervision, H.X. All authors have read and agreed to the published version of the manuscript.

Institutional Review Board Statement: Not applicable.

Informed Consent Statement: Not applicable.

Data Availability Statement: The lidar data can be downloaded from https://figshare.com/articles/dataset/A_month_lidar_results_during_the_experiment/13232615/1, accessed on 18 September 2021. (https://doi.org/10.6084/m9.figshare.13232615.v1, accessed on 18 September 2021).

Conflicts of Interest: The authors declare no conflicts of interest.

References

1. Dessens, J. A Physical Evaluation of a Hail Suppression Project with Silver Iodide Ground Burners in Southwestern France. *J. Appl. Meteorol. Clim.* **1998**, *37*, 1588–1599, doi:10.1175/1520–0450(1998)037<1588:APEOAH>2.0.CO;2.
2. Abshaev, M.T.; Abshaev, A.M.; Zakinyan, R.G.; Zakinyan, A.R.; Wehbe, Y.; Yousef, L.; Farrah, S.; Mandous, A.A. Investigating the feasibility of artificial convective cloud creation. *Atmos. Res.* **2020**, *243*, 104998, doi:10.1016/j.atmosres.2020.104998.
3. Gilbert, D.B.; Boe, B.A.; Krauss, T.W. Twenty seasons of airborne hail suppression in Alberta, Canada. *J. Wea. Modif.* **2016**, *48*, 68–92.
4. Flossmann, A.I.; Manton, M.; Abshaev, A.; Bruintjes, R.; Murakami, M.; Prabhakaran, T.; Yao, Z. Review of Advances in Precipitation Enhancement Research. *Bull. Am. Meteorol. Soc.* **2019**, *100*, 1465–1480, doi:10.1175/BAMS-D-18–0160.1.
5. Dessens, J.; Saìnchez, J.L.; Berthet, C.; Hermida, L.; Merino, A. Hail prevention by ground-based silver iodide generators: Results of historical and modern field projects. *Atmos. Res.* **2016**, *170*, 98–111, doi:10.1016/j.atmosres.2015.11.008.
6. Seto, J.; Tomine, K.; Wakimizu, K.; Nishiyama, K. Artificial cloud seeding using liquid carbon dioxide: Comparison of experimental data and numerical analyses. *J. Appl. Meteorol. Clim.* **2011**, *50*, 1417–1431, doi:10.1175/2011JAMC2592.1.
7. Leisner, T.; Denis, D.; Möhler, O.; Saathoff, H.; Schnaiter, M.; Henin, S.; Stelmaszczyk, K.; Petrarca, M.; Delagrange, R.; Hao, Z.; Lüder,J.; Petit, Y.; Rohwetter, P.; Kasparian, J.; Wolf, J.; Wöste, L. Laser-induced plasma cloud interaction and ice multiplication under cirrus cloud conditions. *Proc. Natl. Acad. Sci. USA* **2013**, *110*, 10106–10110, doi:10.1073/pnas.1222190110.
8. Tan, X.; Qiu, Y.; Yang, Y.; Liu, D.; Lu, X.; Pan, Y. Enhanced growth of single droplet by control of equivalent charge on droplet. *IEEE Trans. Plasma Sci.* **2016**, *44*, 2724–2728, doi:10.1109/TPS.2016.2608832.
9. Tai, Y.; Haoran, L.; Zaki, A.; el Hadri, N. Core/shell microstructure induced synergistic effect for efficient water-droplet formation and cloud-seeding application. *Acs Nano* **2017**, *11*, 12318–12325, doi:10.1021/acsnano.7b06114.
10. Geerts, B. The AgI Seeding Cloud Impact Investigation (ASCII) campaign 2012: Overview and preliminary results. *J. Wea. Modif.* **2013**, *45*, 24–43.
11. Abshaev, M.T.; Abshaev, A.M.; Sulakvelidze, G.K.; Burtsev, I.I.; Malkarova, A.M. *Development of Rocket and Artillery Technology for Hail Suppression*; United Arab Emirates Department of Atmospheric Studies. **2006**, 109–127.
12. Mather, G.K.; Terblanche, D.E.; Steffens, F.E.; Fletcher, L. Results of the South African Cloud-Seeding Experiments Using Hygroscopic Flares. *J. Appl. Meteorol. Clim.* **1997**, *36*, 1433–1447, doi:10.1175/1520–0450(1997)036<1433:ROTSAC>2.0.CO;2.
13. Bruintjes, R.T. A Review of Cloud Seeding Experiments to Enhance Precipitation and Some New Prospects. *Bull. Am. Meteorol. Soc.* **1999**, *80*, 805–820, doi:10.1175/1520–0477(1999)080<0805:AROCSE>2.0.CO;2.

14. DeFelice, T.P.; Axisa, D. Modern and prospective technologies for weather modification activities: Developing a framework for integrating autonomous unmanned aircraft systems. *Atmos. Res.* **2017**, *193*, 173–183, doi:10.1016/j.atmosres.2017.04.024.

15. Wu, X.; Niu, S.; Jin, D.; Sun, H. Influence of natural rainfall variability on the evaluation of artificial precipitation enhancement. *Sci. China Earth Sci.* **2015**, *58*, 906–914, doi:10.1007/s11430–015–5055–0.

16. Parkinson, S.; Kunkel, M.L.; Blestrud, D.R.; Tessendorf, S.A.; Rasmussen, R.M.; Friedrich, K.; French, J.; Xue, L.; Geerts, B.; Rauber, R.M. Wintertime Orographic Cloud Seeding—A Review. *J. Appl. Meteorol. Clim.* **2019**, *58*, 2117–2140, doi:10.1175/jamc-d-18–0341.1.

17. Deshler, T.; Reynolds, D.; Huggins, A. Physical Response of Winter Orographic Clouds over the Sierra Nevada to Airborne Seeding Using Dry Ice or Silver Iodide. *J. Appl. Meteorol. Clim.* **1990**, *29*, 288–330, doi:10.1175/1520–0450(1990)029<0288:PROWOC>2.0.CO;2.

18. Hobbs, P.V.; Lyons, J.H.; Locatelli, J.D.; Biswas, K.R.; Radke, L.F.; Weiss, R.R.; Rangno, A.L. Radar Detection of Cloud-Seeding Effects. *Science* **1981**, *213*, 1250, doi:10.1126/science.213.4513.1250.

19. Chu, X.; Geerts, B.; Xue, L.; Pokharel, B. A Case Study of Cloud Radar Observations and Large-Eddy Simulations of a Shallow Stratiform Orographic Cloud, and the Impact of Glaciogenic Seeding. *J. Appl. Meteorol. Clim.* **2017**, *56*, 1285–1304, doi:10.1175/JAMC-D-16–0364.1.

20. French, J.R.; Friedrich, K.; Tessendorf, S.A.; Rauber, R.M.; Geerts, B.; Rasmussen, R.M.; Xue, L.; Kunkel, M.L.; Blestrud, D.R. Precipitation formation from orographic cloud seeding. *Proc. Natl. Acad. Sci. USA* **2018**, *115*, 1168, doi:10.1073/pnas.1716995115.

21. Sassen, K.; Wang, Z.; Liu, D. Cirrus clouds and deep convection in the tropics: Insights from CALIPSO and CloudSat. *J. Geophys. Res. Atmos.* **2009**, *114*, doi:10.1029/2009JD011916.

22. Sassen, K.; Matrosov, S.; Campbell, J. CloudSat spaceborne 94 GHz radar bright bands in the melting layer: An attenuation-driven upside-down lidar analog. *Geophys. Res. Lett.* **2007**, *34*, L16818, doi:10.1029/2007GL030291.

23. Wang, Z.; Menenti, M. Challenges and Opportunities in Lidar Remote Sensing. *Front. Remote Sens.* **2021**, *2*, 3.

24. Rosenfeld, D.; Zheng, Y.; Hashimshoni, E.; Pohlker, M.L.; Jefferson, A.; Pohlker, C.; Yu, X.; Zhu, Y.; Liu, G.; Yue, Z.; et al. Satellite retrieval of cloud condensation nuclei concentrations by using clouds as CCN chambers. *Proc. Natl. Acad. Sci. USA* **2016**, *113*, 5828–5834, doi:10.1073/pnas.1514044113.

25. Wang, J.; Yue, Z.; Rosenfeld, D.; Zhang, L.; Zhu, Y.; Dai, J.; Yu, X.; Li, J. The Evolution of an AgI Cloud-Seeding Track in Central China as Seen by a Combination of Radar, Satellite, and Disdrometer Observations. *J. Geophys. Res. Atmos.* **2021**, *126*, e2020JD033914, doi:10.1029/2020JD033914.

26. Sassen, K. An Initial Application of Polarization Lidar for Orographic Cloud Seeding Operations. *J. Appl. Meteorol.* **1980**, *19*, 298–304, doi:10.1175/1520–0450(1980)019<0298:AIAOPL>2.0.CO;2.

27. Sassen, K. Depolarization of laser light backscattered by artificial clouds. *J. Appl. Meteorol.* **1974**, *13*, 923–933, doi:10.1175/1520–0450(1974)013<0923:DOLLBB>2.0.CO;2.

28. Cheng, C.; Yi, F. Falling Mixed-Phase Ice Virga and their Liquid Parent Cloud Layers as Observed by Ground-Based Lidars. *Remote Sens.* **2020**, *12*, 2094, doi:10.3390/rs12132094.

29. Bernard, É.; Friedt, J.-M.; Griselin, M. Snowcover Survey over an Arctic Glacier Forefield: Contribution of Photogrammetry to Identify "Icing" Variability and Processes. *Remote. Sens.* **2021**, *13*, 1978, doi:10.3390/rs13101978.

30. Li, H.; Moisseev, D. Two Layers of Melting Ice Particles Within a Single Radar Bright Band: Interpretation and Implications. *Geophys. Res. Lett.* **2020**, *47*, e2020GL087499, doi:10.1029/2020gl087499.

31. Li, H.; Moisseev, D. Melting Layer Attenuation at Ka‐ and W‐Bands as Derived From Multifrequency Radar Doppler Spectra Observations. *J. Geophys. Res. Atmos.* **2019**, *124*, 9520–9533, doi:10.1029/2019jd030316.

32. Hon, K.-K. Predicting Low-Level Wind Shear Using 200-m-Resolution NWP at the Hong Kong International Airport. *J. Appl. Meteorol. Clim.* **2020**, *59*, 193–206, doi:10.1175/jamc-d-19–0186.1.

33. Brooks, B.J.; Davies, F.; Hogan, R.J.; Westbrook, C.D.; Brooks, I.M.; Illingworth, A.J.; O'Connor, E.J. A Method for Estimating the Turbulent Kinetic Energy Dissipation Rate from a Vertically Pointing Doppler Lidar, and Independent Evaluation from Balloon-Borne In Situ Measurements. *J. Atmos. Ocean. Tech.* **2010**, *27*, 1652–1664, doi:10.1175/2010jtecha1455.1.

34. Banakh, V.A.; Smalikho, I.N.; Falits, A.V.; Sherstobitov, A.M. Estimating the Parameters of Wind Turbulence from Spectra of Radial Velocity Measured by a Pulsed Doppler Lidar. *Remote. Sens.* **2021**, *13*, 2071, doi:10.3390/rs13112071.

35. Banakh, V.; Smalikho, I. Lidar Studies of Wind Turbulence in the Stable Atmospheric Boundary Layer. *Remote. Sens.* **2018**, *10*, 1219, doi:10.3390/rs10081219.

36. Banakh, V.A.; Smalikho, I.N.; Falits, A.V. Wind–Temperature Regime and Wind Turbulence in a Stable Boundary Layer of the Atmosphere: Case Study. *Remote. Sens.* **2020**, *12*, 955, doi:10.3390/rs12060955.

37. Li, J.; Shen, C.; Gao, H.; Chan, P.W.; Hon, K.K.; Wang, X. Path integration (PI) method for the parameter-retrieval of aircraft wake vortex by Lidar. *Opt. Express* **2020**, *28*, 4286–4306, doi:10.1364/OE.382968.

38. Gultepe, I.; Heymsfield, A.J. Introduction Ice Fog, Ice Clouds, and Remote Sensing. *Pure Appl. Geophys.* **2016**, *173*, 2977–2982, doi:10.1007/s00024–016–1380–2.

39. Gultepe, I.; Fernando, H.J.S.; Pardyjak, E.R.; Hoch, S.W.; Silver, Z.; Creegan, E.; Leo, L.S.; Pu, Z.; De Wekker, S.F.J.; Hang, C. An Overview of the MATERHORN Fog Project: Observations and Predictability. *Pure Appl. Geophys.* **2016**, *173*, 2983–3010, doi:10.1007/s00024–016–1374–0.

40. Weickmann, A.M.; Senff, C.J.; Tucker, S.C.; Brewer, W.A.; Banta, R.M.; Sandberg, S.P.; Law, D.C.; Hardesty, R.M. Doppler Lidar Estimation of Mixing Height Using Turbulence, Shear, and Aerosol Profiles. *J. Atmos. Ocean. Tech.* **2009**, *26*, 673–688, doi:10.1175/2008jtecha1157.1.

41. Jia, M.; Yuan, J.; Wang, C.; Xia, H.; Wu, Y.; Zhao, L.; Wei, T.; Wu, J.; Wang, L.; Gu, S.Y.; et al. Long-lived high-frequency gravity waves in the atmospheric boundary layer: Observations and simulations. *Atmos. Chem. Phys.* **2019**, *19*, 15431–15446, doi:10.5194/acp-19–15431–2019.

42. Thobois, L.; Cariou, J.P.; Gultepe, I. Review of Lidar-Based Applications for Aviation Weather. *Pure Appl. Geophys.* **2018**, *176*, 1959–1976, doi:10.1007/s00024–018–2058–8.

43. Wang, C.; Xia, H.; Shangguan, M.; Wu, Y.; Wang, L.; Zhao, L.; Qiu, J.; Zhang, R. 1.5 μm polarization coherent lidar incorporating time-division multiplexing. *Opt. Express* **2017**, *25*, 20663–20674, doi:10.1364/OE.25.020663.

44. Wei, T.; Xia, H.; Wu, Y.; Yuan, J.; Wang, C.; Dou, X. Inversion probability enhancement of all-fiber CDWL by noise modeling and robust fitting. *Opt. Express* **2020**, *28*, 29662–29675, doi:10.1364/oe.401054.

45. Wang, C.; Jia, M.; Xia, H.; Wu, Y.; Wei, T.; Shang, X.; Yang, C.; Xue, X.; Dou, X. Relationship analysis of PM2.5 and boundary layer height using an aerosol and turbulence detection lidar. *Atmos. Meas. Tech.* **2019**, *12*, 3303–3315, doi:10.5194/amt-12–3303–2019.

46. Aoki, M.; Iwai, H.; Nakagawa, K.; Ishii, S.; Mizutani, K. Measurements of Rainfall Velocity and Raindrop Size Distribution Using Coherent Doppler Lidar. *J. Atmos. Ocean. Tech.* **2016**, *33*, 1949–1966, doi:10.1175/jtech-d-15–0111.1.

47. Wei, T.; Xia, H.; Hu, J.; Wang, C.; Shangguan, M.; Wang, L.; Jia, M.; Dou, X. Simultaneous wind and rainfall detection by power spectrum analysis using a VAD scanning coherent Doppler lidar. *Opt. Express* **2019**, *27*, 31235–31245, doi:10.1364/OE.27.031235.

48. Kalthoff, N.; Adler, B.; Wieser, A.; Kohler, M.; Träumner, K.; Handwerker, J.; Corsmeier, U.; Khodayar, S.; Lambert, D.; Kopmann, A.; et al. KITcube – a mobile observation platform for convection studies deployed during HyMeX. *Meteorol. Z.* **2013**, *22*, 633–647, doi:10.1127/0941–2948/2013/0542.

49. Träumner, K.; Handwerker, J.; Wieser, A.; Grenzhäuser, J. A Synergy Approach to Estimate Properties of Raindrop Size Distributions Using a Doppler Lidar and Cloud Radar. *J. Atmos. Ocean. Tech.* **2010**, *27*, 1095–1100, doi:10.1175/2010jtecha1377.1.

50. Wei, T.; Xia, H.; Yue, B.; Wu, Y.; Liu, Q. Remote sensing of raindrop size distribution using the coherent Doppler lidar. *Opt. Express* **2021**, *29*, 17246–17257, doi:10.1364/oe.426326.

51. Yuan, J.; Xia, H.; Wei, T.; Wang, L.; Yue, B.; Wu, Y. Identifying cloud, precipitation, windshear, and turbulence by deep analysis of the power spectrum of coherent Doppler wind lidar. *Opt. Express* **2020**, *28*, 37406–37418, doi:10.1364/oe.412809.

52. Harikumar, R.; Sampath, S.; Sasi Kumar, V. Altitudinal and temporal evolution of raindrop size distribution observed over a tropical station using a K-band radar. *Int. J. Remote Sens.* **2011**, *33*, 3286–3300, doi:10.1080/01431161.2010.549853.

53. Wang, L.; Qiang, W.; Xia, H.; Wei, T.; Yuan, J.; Jiang, P. Robust Solution for Boundary Layer Height Detections with Coherent Doppler Wind Lidar. *Adv. Atmos. Sci.* **2021**, *38*, 1920–1928, doi:10.1007/s00376–021–1068–0.

54. Guo, Q.; Lu, F.; Wei, C.; Zhang, Z.; Yang, J. Introducing the New Generation of Chinese Geostationary Weather Satellites, Fengyun-4. *Bull. Am. Meteorol. Soc.* **2017**, *98*, 1637–1658, doi:10.1175/bams-d-16–0065.1.

55. Heymsfield, A.J.; Kennedy, P.C.; Massie, S.; Schmitt, C.; Wang, Z.; Haimov, S.; Rangno, A. Aircraft-Induced Hole Punch and Canal Clouds: Inadvertent Cloud Seeding. *Bull. Am. Meteorol. Soc.* **2010**, *91*, 753–766, doi:10.1175/2009BAMS2905.1.

56. Heymsfield, A.J.; Thompson, G.; Morrison, H.; Bansemer, A.; Rasmussen, R.M.; Minnis, P.; Wang, Z.; Zhang, D. Formation and Spread of Aircraft-Induced Holes in Clouds. *Science* **2011**, *333*, 77, doi:10.1126/science.1202851.

57. Ćurić, M.; Janc, D. Wet deposition of the seeding agent after weather modification activities. *Environ. Sci. Pollut. Res.* **2013**, *20*, 6344–6350, doi:10.1007/s11356–013–1705-y.

58. Ćurić, M.; Janc, D.; Vučković, V.; Kovačević, N. An inadvertent transport of the seeding material as a result of cloud modification. *Adv. Atmos. Sci.* **2009**, *105*, 157–165, doi:10.1007/s00703–009–0040–9.

59. Rosenfeld, D.; Lohmann, U.; Raga, G.B.; O'Dowd, C.D.; Kulmala, M.; Fuzzi, S.; Reissell, A.; Andreae, M.O. Flood or drought: How do aerosols affect precipitation? *Science* **2008**, *321*, 1309–1313, doi:10.1126/science.1160606.

60. Tao, W.-K.; Chen, J.-P.; Li, Z.; Wang, C.; Zhang, C. Impact of aerosols on convective clouds and precipitation. *Rev. Geophys.* **2012**, *50*, RG2001, doi:10.1029/2011rg000369.

61. Lohmann, U. Anthropogenic Aerosol Influences on Mixed-Phase Clouds. *Curr. Clim. Chang. Rep.* **2017**, *3*, 32–44, doi:10.1007/s40641–017–0059–9.

62. DeMott, P.J. Quantitative descriptions of ice formation mechanisms of silver iodide-type aerosols. *Atmos. Res.* **1995**, *38*, 63–99, doi:10.1016/0169–8095(94)00088-U.

63. Farmer, D.K.; Cappa, C.D.; Kreidenweis, S.M. Atmospheric Processes and Their Controlling Influence on Cloud Condensation Nuclei Activity. *Chem. Rev.* **2015**, *115*, 4199–4217, doi:10.1021/cr5006292.

64. Banakh, V.A.; Brewer, A.; Pichugina, E.L.; Smalikho, I.N. Measurements of wind velocity and direction with coherent Doppler lidar in conditions of a weak echo signal. *Atmos. Ocean. Opt.* **2010**, *23*, 381–388, doi:10.1134/s1024856010050076.

65. Shupe, M.D.; Kollias, P.; Matrosov, S.Y.; Schneider, T.L. Deriving mixed-phase cloud properties from Doppler radar spectra. *J. Atmos. Ocean. Tech.* **2004**, *21*, 660–670, doi:10.1175/1520–0426(2004)021<0660:DMCPFD>2.0.CO;2.

66. Pinto, J.O. Autumnal Mixed-Phase Cloudy Boundary Layers in the Arctic. *J. Atmos. Sci.* **1998**, *55*, 2016–2038, doi:10.1175/1520–0469(1998)055<2016:AMPCBL>2.0.CO;2.

67. Ramelli, F.; Henneberger, J.; David, R.O.; Lauber, A.; Pasquier, J.T.; Wieder, J.; Bühl, J.; Seifert, P.; Engelmann, R.; Hervo, M.; et al. Influence of low-level blocking and turbulence on the microphysics of a mixed-phase cloud in an inner-Alpine valley. *Atmos. Chem. Phys.* **2021**, *21*, 5151–5172, doi:10.5194/acp-21–5151–2021.

68. Iguchi, T.; Matsui, T.; Tao, W.-K.; Khain, A.P.; Phillips, V.T.J.; Kidd, C.; L'Ecuyer, T.; Braun, S.A.; Hou, A. WRF–SBM Simulations of Melting-Layer Structure in Mixed-Phase Precipitation Events Observed during LPVEx. *J. Appl. Meteorol. Clim.* **2014**, *53*, 2710–2731, doi:10.1175/JAMC-D-13–0334.1.

69. Yu, G.; Verlinde, J.; Clothiaux, E.E.; Chen, Y.S. Mixed-phase cloud phase partitioning using millimeter wavelength cloud radar Doppler velocity spectra. *J. Geophys. Res. Atmos.* **2014**, *119*, 7556–7576, doi:10.1002/2013jd021182.

70. Ćurić, M.; Janc, D.; Vučković, V. Precipitation change from a cumulonimbus cloud downwind of a seeded target area. *J. Geophys. Res.* **2008**, *113*, doi:10.1029/2007jd009483.

71. Tian, J.; Dong, X.; Xi, B.; Williams, C.R.; Wu, P. Estimation of liquid water path below the melting layer in stratiform precipitation systems using radar measurements during MC3E. *Atmos. Meas. Tech.* **2019**, *12*, 3743–3759, doi:10.5194/amt-12–3743–2019.

72. Qiu, J.; Xia, H.; Shangguan, M.; Dou, X.; Li, M.; Wang, C.; Shang, X.; Lin, S.; Liu, J. Micro-pulse polarization lidar at 1.5 mum using a single superconducting nanowire single-photon detector. *Opt. Lett.* **2017**, *42*, 4454–4457, doi:10.1364/OL.42.004454.